Quantifying local rearrangements in three-dimensional granular materials: Rearrangement measures, correlations, and relationship to stresses

Chongpu Zhai

State Key Laboratory for Strength and Vibration of Mechanical Structures, School of Aerospace, Xi'an Jiaotong University, Xi'an, China
and Department of Mechanical Engineering, Johns Hopkins University, Baltimore, Maryland 21218, USA

Nahuel Albayrak

Hopkins Extreme Materials Institute, Johns Hopkins University, Baltimore, Maryland 21218, USA

Jonas Engqvist and Stephen A. Hall

Division for Solid Mechanics, Lund University, Lund 22100, Sweden

Jonathan Wright and Marta Majkut

ESRF—The European Synchrotron, Grenoble 38000, France

Eric B. Herbold

Atmospheric, Earth, & Energy Division, Lawrence Livermore National Laboratory, Livermore, California 94550, USA

Ryan C. Hurley[*]

Department of Mechanical Engineering, Johns Hopkins University, Baltimore, Maryland 21218, USA
and Hopkins Extreme Materials Institute, Johns Hopkins University, Baltimore, Maryland 21218, USA

Quantifying the ways in which local particle rearrangements contribute to macroscopic plasticity is one of the fundamental pursuits of granular mechanics and soft matter physics. Here we examine local rearrangements that occur naturally during the deformation of three samples of 3D granular materials subjected to distinct boundary conditions by employing *in situ* x-ray measurements of particle-resolved structure and stress. We focus on five distinct rearrangement measures, their statistics, interrelationships, contributions to macroscopic deformation, repeatability, and dependence on local structure and stress. Our most significant findings are that local rearrangements (1) are correlated on a scale of three to four particle diameters, (2) exhibit volumetric strain-shear strain and nonaffine displacement-rotation coupling, (3) exhibit correlations that suggest either rearrangement repeatability or that rearrangements span multiple steps of incremental sample strain, and (4) show little dependence on local stress but correlate with quantities describing local structure, such as porosity. Our results are presented in the context of relevant plasticity theories and are consistent with recent findings suggesting that local structure may play at least as important of a role as local stress in determining the nature of local rearrangements.

I. INTRODUCTION

Macroscopic plasticity in granular materials occurs due to the accumulation of numerous local particle rearrangements [1,2]. This feature of plasticity is shared with other amorphous materials [3,4], including metallic glasses [5], colloids [4], and emulsions [6]. The locations and magnitudes of local rearrangements in these materials are thought to be related to a combination of structural defects and the local stress state. However, these structural defects and stress states have been challenging to identify in amorphous materials [7–11].

In contrast, dislocations are known to be structural defects causing plasticity in metals [12].

A major motivation for characterizing local rearrangement events in amorphous materials is to support the development and calibration of continuum models that capture the role of these rearrangements in macroscopic plasticity. Free volume theories [13], elastoplastic models [2], shear transformation zone theory (STZ) [14], and soft glassy rheology theory (SGR) [15] are among the popular models linking local rearrangements and macroscopic plasticity in amorphous materials. These models rely on assumptions regarding the sizes, induced strains, frequencies, and interactions of rearrangement events, much of which has been furnished primarily by numerical simulations. For instance, nonaffine particle translation in metallic glasses and granular

―――――――
[*]rhurley6@jhu.edu

materials [8,14,16], particle rotations in granular materials [17,18], and strain fluctuations in colloids [5,16] have been studied extensively using molecular dynamics and discrete element method simulations. A small number of experiments with *in situ* structure measurements have also provided rich data on rearrangements in granular materials. For instance, cyclic compression and shear of submerged 3D granular media has revealed that macroscopic plasticity is related to irreversible particle rotations linked to alterations of contact forces and grain stresses [19,20]. Macroscopic compaction of vibrated 3D granular media has been shown to be accommodated by local transitions through crystal-like structural configurations [21–23]. Shear band nucleation and propagation in biaxially compressed granular materials has been linked to isolated events inducing local strains consistent with the Eshelby solution of a local plastic transformation [1,24].

Recent research has moved closer to identifying local structural motifs and stress states causing rearrangements in amorphous materials. Machine learning has been applied to numerical and experimental data to show that the local structure is related to local rearrangements in glasses [25], polycrystals [26], low-dimensional films [27], and granular materials [28]. For instance, support vector machines (SVMs), operating on a large set of local structure functions only, have classified regions of a granular material as "soft," or prone to rearrangement or nonaffine motion [4,8].

In this paper we use particle-resolved structure and stress tensor data obtained using *in situ* x-ray tomography and diffraction measurements [29,30] on deforming granular materials to examine local rearrangements. The local rearrangements we examine occur naturally throughout each of three samples that we subject to distinct boundary conditions. We examine five measures of local particle rearrangements, focusing on the statistics, spatial correlations, strain coupling, contributions to macroscopic deformation, repeatability, and dependence on local structure and stress. Our analysis suggests that (1) local rearrangements are correlated at a scale of about three to four particle diameters, (2) rearrangements exhibit volumetric strain-shear strain and nonaffine displacement-rotation coupling, (3) rearrangements exhibit correlations that suggest either memory effects (i.e., rearrangements can occur in the same location twice) or that individual rearrangement events may occur over multiple increments of sample strain, and (4) rearrangements show little dependence on local stress but correlate with quantities describing local structure. We discuss the implications of our findings for STZ theory and elastoplastic models of granular rheology.

Section II provides a description of the experimental data used for analysis in the remainder of the paper. Section III includes a description of rearrangement measures, their cross-correlations, contributions to macroscopic deformation, repeatability, and dependence on local structure and stress. Section IV offers a discussion and conclusions.

II. EXPERIMENTS

All experiments examined in this paper took place at beamline ID11 of the European Synchrotron Radiation Facility (ESRF). Experiments were performed on three samples, each composed of single-crystal ruby spheres (Sandoz Fils SA) with an approximate diameter of 140–150 μm and a uniform roughness below 0.008 μm (arithmetic mean height deviation). The three samples A, B, and C investigated in this study are corresponding to uniaxial, hydrostatic, and triaxial loading conditions, respectively. Sample A, shown in Fig. 1(a) and composed of 886 ruby spheres, was prepared by pouring particles into a 1.5 mm inner diameter aluminum cylinder. This sample was monotonically compressed via application of incremental vertical strain (a uniaxial strain test), except for a brief unloading that is not analyzed further here. Samples B and C, shown in Figs. 1(b) and 1(c), respectively, were composed of 877 and 1667 ruby spheres and were prepared by pouring particles into 1.5 mm inner diameter polymer sleeves. These samples were first subjected to a hydrostatic confinement of 3 MPa by pressurizing a fluid surrounding their polymer sleeves. They were subsequently monotonically compressed via application of incremental vertical strain. Load steps reported for these samples in this paper begin after the application of 3 MPa confinement. The polymer sleeve used for sample B was significantly stiffer than that used for sample C and thus caused a lateral confining stress above the 3 MPa imposed by the surrounding confining fluid (see [31]). Sample B was therefore similar to a hydrostatic stress test while Sample C was closer to a traditional triaxial stress test.

A. XRCT and 3DXRD measurements

After each increment of vertical strain, samples were rotated 180° in 0.1° increments to capture 1800 radiographs that were used to construct XRCT images in PyHST [32]. The resulting XRCT images had a resolution of 1.54³ μm³ per voxel. Figures 1(a), 1(b), and 1(c) show the XRCT images at load step 1 for each sample. After the 180° rotation, samples were rotated 360° in 0.125° increments to capture 1440 2D diffraction patterns that were used in 3D x-ray diffraction (3DXRD) analysis in ImageD11 [33]. 3DXRD analysis yielded per-particle strain tensors, orientations, and positions for each particle that generated at least 24 Bragg peaks in the 2D diffraction patterns (between 95% and 100% of particles found in XRCT images at each load step). 3DXRD analysis yielded per-particle volume-averaged strain tensors with a resolution of 10^{-4} per on-diagonal and 5×10^{-5} per off-diagonal tensor component [30,34], particle orientations with a resolution of 0.05° or better [34], and particle positions with a resolution of around 10 μm. From per-particle volume-averaged strain tensors, per-particle stresses were calculated using the known stiffness tensor of ruby ($C_{11} = 496.8$ GPa, $C_{33} = 498.1$ GPa, $C_{12} = 163.6$ GPa, $C_{13} = 110.9$ GPa, $C_{14} = 23.5$ GPa, $C_{66} = (C_{11} - C_{12})/2$). Individual particle stress tensors had a resolution of 50 MPa per on-diagonal tensor component and 23 MPa per off-diagonal tensor component [35]. Registration was performed between particle centers in XRCT and 3DXRD measurements and per-particle stress tensors and orientations were subsequently assigned to each particle in XRCT images.

B. Global and local strains

Global sample strains, ϵ_{zz}^S, were determined by manually locating the stainless steel platens in contact with the top
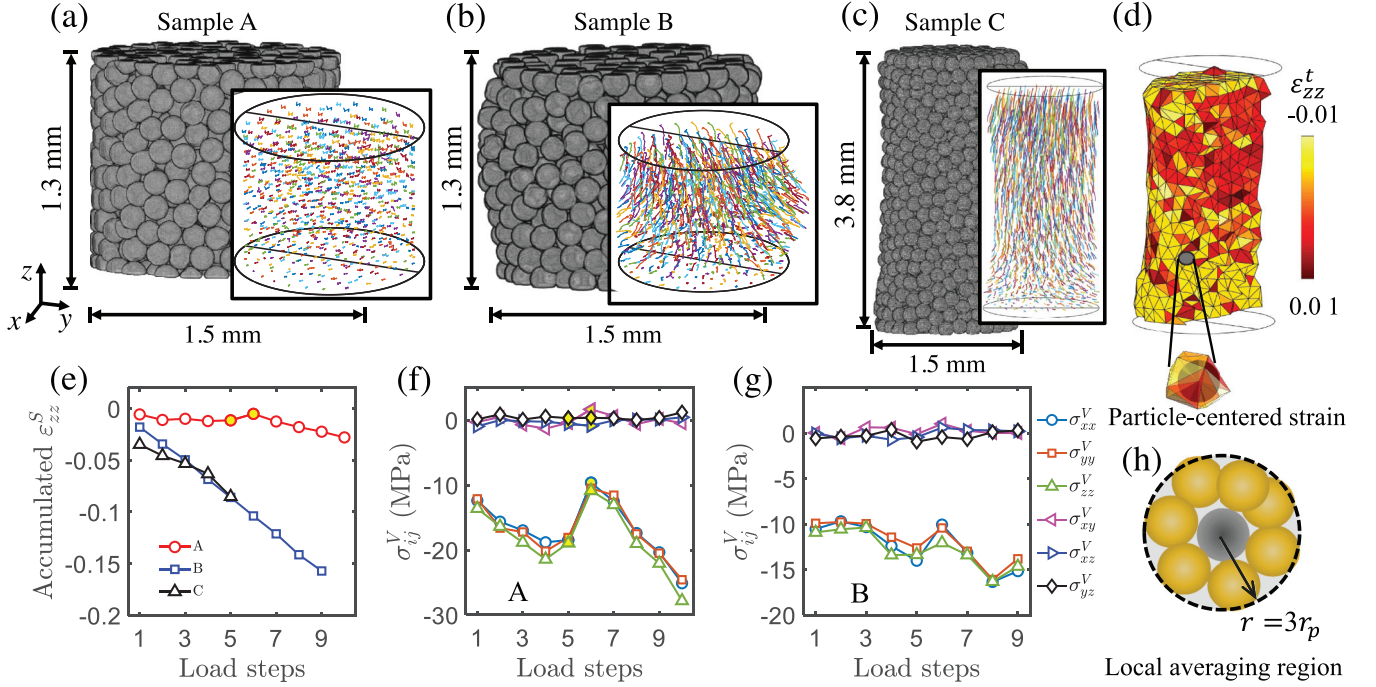
FIG. 1. [(a)–(c)] XRCT reconstructions of Samples A, B, and C, respectively. Insets show particle kinematics from the start to the end of each experiment. Each particle center is given a distinct color in these insets. (d) Local tetrahedron-based strains calculated using Eq. (2) for particles not contacting boundaries in load step 2 of Sample C. The tetrahedron-based vertical strain is indicated by the tetrahdron's color. The tetrahedrons used to calculate particle-centered strain are illustrated in the inset. (e) The accumulated global sample strain, ϵ_{zz}^S, as a function of load step for all samples. [(f), (g)] Average sample stresses obtained from Eq. (3). (h) An illustration of a local averaging region of radius $r = 3r_p$.

and bottom of samples in XRCT images. The vertical sample strains are shown in Fig. 1(e). Symbols in this figure indicate the strains at which XRCT and 3DXRD measurements were made.

To obtain each particle's kinematics, XRCT images were first segmented to separate individual particles and obtain their center of mass positions [31]. Position resolution with this approach is thought to be as good as 0.05 pixels [36]. To track 3D particle displacements, u_i (a displacement vector in index notation), the distance between the center of mass position of each particle in a given load step and all particles in the preceding load step was first calculated. The particle in the preceding load step with the smallest distance was assumed to be the same particle. Particle displacements throughout each experiment are shown as insets in Figs. 1(a), 1(b), and 1(c).

To calculate local strains, a Voronoi tessellation was computed at each load step using particle centers and radii [37] and was subsequently used to construct the Delaunay triangulation, the dual network to the Voronoi tessellation [38]. The displacement gradient of each tetrahedron t in the Delaunay triangulation, $u_{i,j}^t$, was then calculated by

$$u_{i,j}^t = \frac{1}{V_t} \sum_{k=1}^{4} u_i^k a_j^k, \qquad (1)$$

where V_t is the tetrahedron volume, k is a particle center forming the tetrahedron, u_i^k is the displacement of the particle at node k between consecutive load steps of an experiment, and a_j^k is a vector with a magnitude equal to the area of the tetrahedron face not containing node k divided by the

space dimension (three in three dimensions), pointing toward the tetrahedron interior and perpendicular to the tetrahedron face not containing node k [39]. The infinitesimal strain and rotation tensors for each tetrahedron were then computed as

$$\varepsilon_{ij}^t = \frac{1}{2}\left(u_{i,j}^t + u_{j,i}^t\right) \text{ and } \omega_{ij}^t = \frac{1}{2}\left(u_{i,j}^t - u_{j,i}^t\right). \qquad (2)$$

Local strains between load steps 2 and 3 of Sample C are illustrated on a Delaunay triangulation in Fig. 1(d).

C. Sample stresses

Volume-averaged sample stress, σ_{ij}^V, was calculated for each sample at each load step by

$$\sigma_{ij}^V = \frac{N_T}{N_{\text{XRD}}} \frac{1}{V_S} \sum_{k=1}^{N_{\text{XRD}}} \sigma_{ij}^k V_k, \qquad (3)$$

where N_T is the total number of particles found in XRCT images, N_{XRD} is the number of particles with stresses from 3DXRD analysis, V_S is the sample volume, σ_{ij}^k is particle k's stress tensor from 3DXRD, and V_k is particle k's volume from XRCT. The volume-averaged stress evolution for Samples B and C are shown in Fig. 1(f) and 1(g), respectively. Experimental challenges made stress tensors for Sample C unreliable, and they are therefore not examined further here.

D. Interparticle forces

Interparticle forces were inferred at each load step of experiments on Samples A and B, as described in [31]. Force inference employed the optimization procedure proposed in

[29] and the assumptions of noncohesive forces and a friction coefficient of 0.2 for particle-particle and particle-aluminum contacts and 0.4 for particle-polymer-sleeve contacts. The force inference procedure required particle volumes, contact locations, and contact normal vectors from XRCT images, and per-particle stress tensors from 3DXRD data. Contacts were identified by first identifying a voxel in segmented XRCT images for each sample as a contact if the 26-voxel neighborhood around it contained two distinct particles. The center of the resulting voxel cloud for a given pair of particles was considered to be the contact location. The contact normal was assumed to be parallel to a vector pointing between the corresponding particles' centers. The reader is directed to [31] for a visualization of forces at multiple load steps of the experiments on Samples A and B, and for a demonstration of their use in calculating per-contact energy dissipation. The reader is directed to [40] for the particle positions, and contact positions and orientations for all samples, as well as the particle stress tensors and forces for Samples A and B.

III. REARRANGEMENT ANALYSIS

A. Rearrangement definitions

We computed five measures of local rearrangements and deformation at each load step of each experiment. These measures are inspired by prior studies examining local rearrangements in metallic glasses and granular materials, for instance in the context of STZ theory [14,16,41]. Three of these measures, local shear ($\gamma_{\max}$), dilation (ϵ_+), and contraction (ϵ_-), are based entirely on the local strains described in Sec. II B. These local measures are particularly relevant to STZ theory and elastoplastic models [14,41]; such theories assume that macroscopic strain is accommodated by local, isolated strain events with certain principal directions and magnitudes. One of the remaining two measures of local rearrangement quantifies nonaffine particle translation and is the popular $D_{\min}^2$ metric introduced in the original paper describing STZ theory [14]. The final measure of local rearrangement quantifies relative rotation of a particle with respect to its neighbors and the rigid-body rotation of the material. This rearrangement measure is intended to capture relative rotations, which are known to be a signature of plasticity in cyclically sheared granular media but may not be identified by analyzing local strains or $D_{\min}^2$ [19,20].

We first define local averaging regions as regions of radius $r = Nr_p$, where N is an integer, centered on the center of mass of a particle with mean radius r_p. Prior work in metallic glasses [14], colloidal glasses [5], and granular materials [8] suggest that local, isolated rearrangement events can be identified with $D_{\min}^2$ when the local averaging region under consideration is between $r = 2r_p$ and $r = 3r_p$. We therefore choose $r = 3r_p$ for most analysis in this paper and note that changing r between $2r_p$ and $4r_p$ does not qualitatively change any of our results. A schematic illustration of a local averaging region of radius $r = 3r_p$ is shown in Fig. 1(h). Figure 2 provides a schematic illustration of the rearrangement measures defined in this subsection, also provided for $r = 3r_p$.
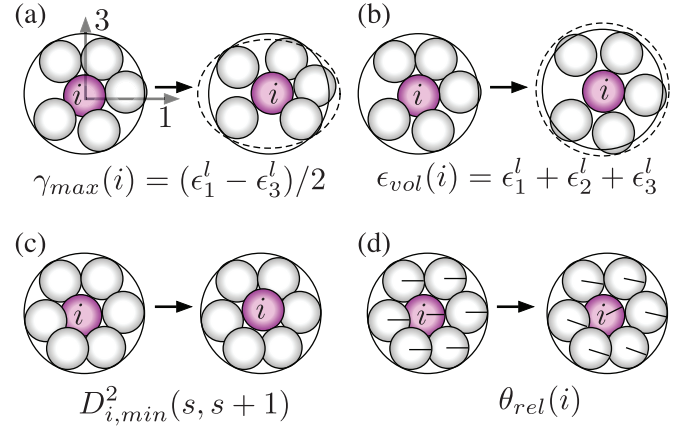

FIG. 2. Illustration of particle rearrangements in local averaging regions centered around particle *i*. (a) Maximum shear strain, $\gamma_{\max}$. (b) Volumetric strain, ϵ_{vol}. (c) Nonaffine motion, $D_{\min}^2$. (d) Relative rotation, θ. All rearrangements defined in the text.

To compute local shear, dilation, and contraction, we first compute the strains in all tetrahedrons for which a particle is a node, which we call the particle-centered strain [38], as

$$\epsilon_{ij}^c = \frac{1}{V_c} \sum_{t=1}^{N_t^c} \epsilon_{ij}^t V_t, \tag{4}$$

where t is the index of a tetrahedron for which a particle is a node, N_t^c is the number of all such tetrahedrons for particle c, V_t is the volume of tetrahedron t, ϵ_{ij}^t is the strain tensor of tetrahedron t, and $V_c = \sum_{t=1}^{N_t^c} V_t$ is the sum of all tetrahedrons with volumes V_t contact particle c. An illustration of the tetrahedrons involved in calculating the particle-centered strain for a particle within Sample C is given in the inset to Fig. 1(d).

Next, we compute the local strain in the averaging region by

$$\epsilon_{ij}^l = \frac{1}{V_l} \sum_{c=1}^{N_p^e} \epsilon_{ij}^c V_c, \tag{5}$$

where c is the index of a particle partially or fully within the local averaging region, V_c is the volume of the particle within the region, N_p^c is the number of particles fully or partially in the region, and $V_l = \sum_{c=1}^{N_p^e} V_c$ is the sum of all particle volumes within the local averaging region. For particles partially in the local averaging region, V_c is calculated using a sphere-sphere intersection formula [42]. Finally, we compute the local shear, dilation, and contraction in the local averaging region as

$$\gamma_{\max} = \frac{\epsilon_1^l - \epsilon_3^l}{2},$$
$$\epsilon_{\mathrm{vol}} = \epsilon_1^l + \epsilon_2^l + \epsilon_3^l, \tag{6}$$

where ϵ_1^l, ϵ_2^l, and ϵ_3^l are the principal strains in the local averaging region, calculated from an eigenvalue decomposition of ϵ_{ij}^l. A local region can exhibit either a local dilation ($\epsilon_{\mathrm{vol}} > 0$), in which case it is labeled ϵ_+, or a local contraction $\epsilon_{\mathrm{vol}} < 0$, in which case it is labeled ϵ_-.

To compute $D_{\min}^2$ for particle i between two load steps, s and $s+1$, we calculate

$$D_{i,min}^2(s, s+1) = \min_{\epsilon_{kl}} \frac{1}{N_p^e} \sum_{j=1}^{N_p^e} \left[\Delta d_k^{ij}(s+1) - \epsilon_{kl} d_l^{ij}(s) \right],$$
(7)

where $d_k^{ij}(s) = r_j(s) - r_i(s)$ is the relative position of particles i and j at step s, $\Delta d_k^{ij}(s+1) = d_k^{ij}(s+1) - d_k^{ij}(s)$, ϵ_{kl} is a strain tensor, and N_p^j is the number of particles j around a central particle i in the local averaging region [8,14,16]. Minimization in Eq. (7) is performed over the strain tensor ϵ_{kl}. This definition of $D_{\min}^2$ is analogous to the one proposed in [8,16].

Finally, to compute the relative rotation of a particle, θ_{rel}, with respect to its neighbors and the surrounding rigid-body rotation, we employ both 3DXRD and rigid-body rotations calculated using Eq. (2). A rotation matrix describing the rotation of particle $i's$ crystal orientation is denoted $\mathbf{R}^{xrd}(i)$. This rotation maps a vector aligned with a crystallographic direction in a particle to the same crystallographic direction in the next load step; it includes both the relative rotation of the particle and the local rigid-body rotation of the material. To account for the rigid-body rotation, we first calculate the particle-centered rigid-body rotation analogously to Eq. (4),

$$\omega_{ij}^{V_e} = \frac{1}{V_c} \sum_{t=1}^{N_t^c} \omega_{ij}^t V_t.$$
(8)

From $\omega_{ij}^{V_e}$, we formulate the rotation matrix describing rigid-body rotation associated with $\omega_{ij}^{V_e}$ for particle i as $\mathbf{R}^{\text{cell}}(i) \approx \omega_{ij}^{V_e} + \mathbf{I}$, where $\mathbf{I}$ is the 3D identity matrix. The product $\mathbf{R}^{\text{cell}}(i)^{-1} \mathbf{R}^{xrd}(i)$ removes the rigid-body rotational component from $\mathbf{R}^{xrd}(i)$, leaving only the rotation of a particle in a local frame which rotates rigidly with the material. Finally, we evaluate the rotation matrix describing the *relative* rotation of particle i to its neighbor j by

$$\mathbf{R}^{ij} = (\mathbf{R}^{\text{cell}}(j)^{-1} \mathbf{R}^{xrd}(j))^{-1} \mathbf{R}^{\text{cell}}(i)^{-1} \mathbf{R}^{xrd}(i).$$
(9)

If particles i and j each rotate identically and share the same local rigid-body rotation, then $\mathbf{R}^{xrd}(i) = \mathbf{R}^{xrd}(j)$ and Eq. (9) yields $\mathbf{R}^{ij} = \mathbf{I}$. If, on the other hand, the particles rotate relative to one another, have differing local rigid-body rotations, or both, Eq. (9) will not be the identity matrix. An axis-angle calculation from Eq. (9) yields the rotation of particle i relative to particle j, θ_{rel}^{ij}, and the final relative rotation of particle i in a local region is given by

$$\theta_{\text{rel}}(i) = \frac{1}{N_p^e} \sum_{j=1}^{N_p^j} \theta_{\text{rel}}^{ij},$$
(10)

where N_p^j is the number of particles in the local averaging region.

We note that sums in Eqs. (5), (7), and (9) are taken over all particles, including those contacting boundaries. However, because we analyze local regions with $r = 3r_p$ in this paper, we do not consider rearrangement measures centered on particles contacting boundaries in any statistical analysis throughout the paper. Ignoring such regions prevents local regions from extending into the void space outside of the samples and also eliminates some of the influence of boundaries on rearrangements, which may vary across samples because of the differences in boundary material (aluminum in Sample A and membranes in Samples B and C).

B. Rearrangement normalization and statistics

To compare rearrangement measures across samples and load step increments, we first normalize them. Letting $e(i)$ represent any of the five rearrangement measures around particle i calculated between any two consecutive load step increments, the normalized measure is calculated by

$$e^{(n)}(i) = \frac{e(i) - \langle e(i) \rangle}{\text{std}(e(i))},$$
(11)

where $\langle e(i) \rangle$ is the average rearrangement magnitude over all particles considered within a specific sample and load step increment and $\text{std}(e(i))$ is the standard deviation of rearrangement magnitude over the same particles.

Figure 3 illustrates the distributions of normalized rearrangement measures using $r = 3r_p$, calculated for all particles not in contact with sample boundaries. Each curve in Fig. 3 represents the statistics of rearrangements in each sample between two consecutive load steps. All normalized rearrangement measures greater than zero represent rearrangements with magnitudes that are greater than the mean in a set of consecutive load steps; normalized rearrangement measures less than zero represent rearrangements with magnitude less than the mean. Although samples and load step increments feature distinct incremental strains in Fig. 1(e), normalization appears to collapse $\gamma_{\max}^{(n)}$ and $\epsilon_{\text{vol}}^{(n)}$ onto like curves for all samples and load step increments. Normalization collapses $\theta_{\text{rel}}^{(n)}$ and $D_{\min}^{2(n)}$ onto like curves but with more variability than the collapsed curves for $\gamma_{\max}^{(n)}$ and $\epsilon_{\text{vol}}^{(n)}$.

We examine the relative broadness and the variance of the normalized distributions in Figs. 3(e) and 3(f), which illustrate the slope of exponential fits to the shaded portions of the curves in Figs. 3(a)–3(d). We note that the tails of the distributions in Figs. 3(a)–3(d) are only approximately exponential. The exponents in Fig. 3(e) and 3(f) are given as a function of the increment of global sample strain between consecutive load steps s and $s+1$ analyzed for rearrangements, $\Delta\epsilon_{zz}^S(s, s+1)$, or as a function of the hydrostatic sample stress, $\sigma_h^V(s) = \frac{1}{3}\sigma_{ii}$, in the first of consecutive load steps analyzed. Exponents are calculated by first binning the counts of normalized rearrangements for a given sample and load step in bins of width 0.05 to 0.6 (in increments of 0.05) within the shaded regions of Fig. 3(a)–3(d), and then performing least-squares fitting to a straight line in log-linear space. Symbols in Fig. 3(e) and 3(f) represent the average of the 12 resulting exponents for each sample and load steps; error bars represent the standard deviation of all exponents for different bin sizes.

Figures 3(e) and 3(f) illustrate that $\epsilon_+^{(n)}$ decays most steeply, having the largest exponent by absolute value, and is therefore the most homogeneous of all the rearrangements. This finding may be related to the compression boundary conditions in all experiments, which may limit the extreme values of $\epsilon_+^{(n)}$ that may be achieved. Figures 3(e) and 3(f) also show that the
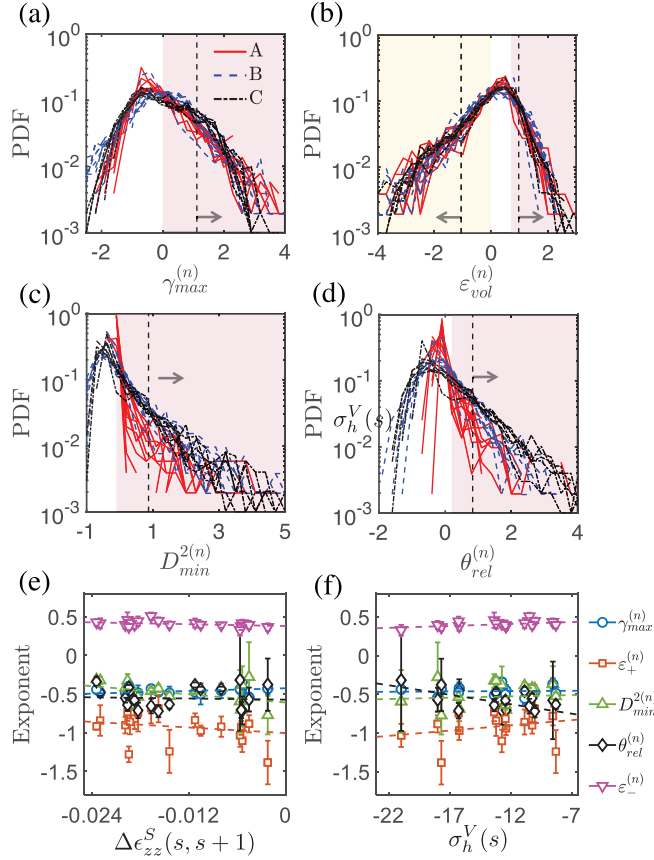
FIG. 3. Probability distributions of normalized rearrangements across all load samples and load steps. Each curve corresponds to rearrangements calculated between consecutive load steps s and $s + 1$. (a) $\gamma_{max}^{(n)}$, (b) $\epsilon_{vol}^{(n)}$, (c) $D_{min}^{2(n)}$, and (d) $\theta_{rel}^{(n)}$. Shaded regions are used to compute exponents of exponential fits described in the text. Dashed vertical lines and arrows indicate the 15% largest rearrangements by magnitude for each rearrangement measure. Panel (b) features two shaded regions and two dashed lines and arrows because we consider ϵ_- ($\epsilon_{vol} < 0$) and ϵ_+ ($\epsilon_{vol} > 0$), as described in the text. The exponents from exponential fitting are given in (e) as a function of incremental sample strain between consecutive load steps, $\Delta\epsilon_{zz}^S(s, s + 1)$, and (f) as a function of the hydrostatic sample stress at the first load step of consecutive steps used for calculating rearrangements, $\sigma_h^V(s)$.

other four rearrangements exhibit roughly similar exponents (around 0.5 in absolute value) and therefore similar heterogeneity.

The dashed curves in Fig. 3(e) and 3(f) are least-squares fitted slopes between the exponents calculated for every load step increment of every sample and $\Delta_{zz}^S(s, s + 1)$ or $\sigma_h^V(s)$. Slight trends towards more heterogeneous distributions (exponents closer to zero) are observed for $\theta_{rel}^{(n)}$, $D_{min}^{2(n)}$, and $\epsilon_+^{(n)}$ in Fig. 7(e) below as $\Delta\epsilon_{zz}^S(s, s + 1)$ increases in magnitude, suggesting that for larger incremental strains it may be increasingly common to find rearrangements significant above the mean. The opposite trend is observed for $\epsilon_+^{(n)}$ in Fig. 3(f) as $\sigma_h^V(s)$ decreases: under more intense hydrostatic confinement, $\epsilon_+^{(n)}$ becomes more homogeneous. On the other hand, $\theta_{rel}^{(n)}$ becomes more heterogeneous with decreasing σ_h^V, suggesting

that more intense hydrostatic confinement my cause more significant, localized relative rotation events.

C. Rearrangement spatial distributions and length scales

Figures 4–6 illustrate the location and magnitude of rearrangements within Samples A, B, and C. For each image in Fig. 4, rearrangements are calculated using consecutive load steps. Particles centered in local averaging regions featuring the largest 15% (by magnitude) $\gamma_{max}^{(n)}$, $\epsilon_+^{(n)}$, or $D_{min}^{2(n)}$, and the most negative $\epsilon_-^{(n)}$ are rendered with color representing their relative magnitude within the 15% tail of the distribution; the typical location of these top 15% rearrangements within the tails of the distributions are shown with dashed lines and arrows in Fig. 3. Particles centered on local averaging regions for which rearrangements are calculated but are not in the largest (or most negative) 15% are rendered in translucent grey. Particles touching boundaries, included in calculations of local rearrangements but not featured at the center of local averaging regions, are rendered in translucent blue.

Rearrangements demonstrate variable spatial clustering and isolation depending on the sample, load step, and rearrangement measure. For instance, in Samples A (Fig. 4) and C (Fig. 6), $\gamma_{max}^{(n)}$ and $\epsilon_-^{(n)}$ cluster near the top or lateral boundaries across most load steps. On the other hand, $D_{min}^{2(n)}$ does not repeatedly cluster in any sample, but demonstrates both spatial clustering and isolation in all samples depending on load step. Some localized rearrangements clearly span multiple load steps or occur in repeatable locations across multiple load steps, as demonstrated by regions of large $D_{min}^{2(n)}$ and $\theta_{rel}^{(n)}$ highlighted with black arrows in Fig. 4 for Sample A, by regions of large $\epsilon_+^{(n)}$ highlighted with black arrows in Fig. 5 for Sample B, and by regions of large $\epsilon_-^{(n)}$ highlighted with black arrows in Fig. 6 for Sample C. Such observations are consistent with those from the prior studies which find that STZs or avalanches identified by D_{min}^2 can span multiple time steps of a simulation and can activate nearby STZs and avalanches [14,43]. Some rearrangement measures are also spatially correlated with others, as is the case for $D_{min}^{2(n)}$ and $\theta_{rel}^{(n)}$ in Sample C, as shown in Fig. 6. The following paragraphs and subsections examine spatial autocorrelations of rearrangements, coupling between rearrangements, and repeatability of rearrangements in more quantitative terms.

To confirm that rearrangements are not significantly correlated beyond $r = 3r_p$, we calculate the spatial autocorrelation between rearrangements occurring in consecutive load step increments, s to $s + 1$, within a certain distance of one another. We first order rearrangements calculated between steps s and $s + 1$ for each sample from largest (1%) to smallest (100%) for $\gamma_{max}^{(n)}$, $\epsilon_+^{(n)}$, $D_{min}^{2(n)}$, and $\theta_{rel}^{(n)}$, and from most negative (1%) to most positive (100%) for $\epsilon_-^{(n)}$. Within only the largest 15%, 30%, or 45% of rearrangements for $\gamma_{max}^{(n)}$, $\epsilon_+^{(n)}$, $D_{min}^{2(n)}$, and $\theta_{rel}^{(n)}$ and most negative 15%, 30%, or 45% of rearrangements for $\epsilon_-^{(n)}$, we compute the mean-squared value $\langle(e^{(n)})^2\rangle$, where e corresponds to any of the five rearrangement measures. Next, we compute the covariance of the rearrangement measure for each particle pair i and j within the largest (or most negative for $\epsilon_-^{(n)}$) 15%, 30%, or 45% of

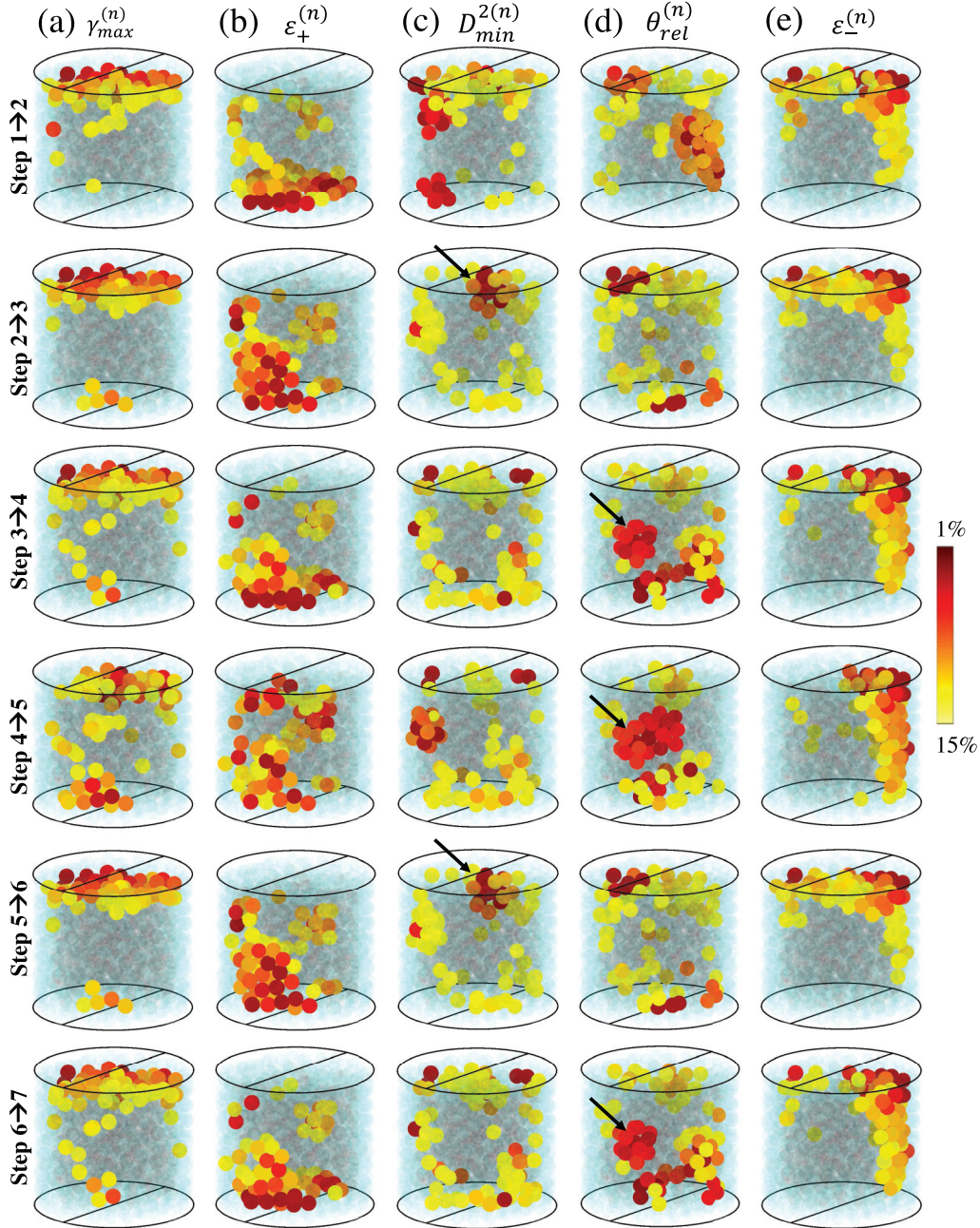FIG. 4. Rendering of Sample A with particle-centered regions exhibiting the largest 15% of rearrangements (or most negative 15% for $\epsilon_-^{(n)}$) by magnitude for six load step increments. (a) $\gamma_{max}^{(n)}$, (b) $\epsilon_+^{(n)}$, (c) $D_{min}^{2(n)}$, (d) $\theta_{rel}^{(n)}$, and (e) $\epsilon_-^{(n)}$. Colors indicate magnitude of normalized rearrangement from the largest (1%) to the smallest (15%) within the top 15%. Particles centered on local averaging regions for which rearrangements are calculated are rendered in translucent gray. Particles touching boundaries, included in calculations of local rearrangements but not featured at the center of local averaging regions, are rendered in translucent blue. Black arrows highlight regions that experience recurring rearrangements between distinct load step pairs or rearrangement events that span multiple load steps, as described in Sec. III F.

rearrangements with centers separated by less than R_{sc} in step s as $\langle (e_i^{(n)} - \langle e^{(n)} \rangle)(e_j^{(n)} - \langle e^{(n)} \rangle) \rangle$. Finally, we divide the covariance by the mean-squared value to yield the spatial correlation coefficient

$$S_{\text{corr}}(R_{sc}, s, s+1) = \frac{\langle (e_i^{(n)} - \langle e^{(n)} \rangle)(e_j^{(n)} - \langle e^{(n)} \rangle) \rangle}{\langle (e^{(n)})^2 \rangle}. \quad (12)$$

Figure 7 shows the spatial autocorrelation coefficient for the top 15%, 30%, and 45% of rearrangements as a function of R_{sc}/r_p for load step 9 of Sample A [in Figs. 7(a), 7(b), and 7(c)], for load step 8 of Sample B [in Figs. 7(d), 7(e), and 7(f)], and for load step 3 of Sample C [in Figs. 7(g), 7(h), and 7(i)]. These load steps were chosen arbitrarily but were found to be representative of the autocorrelation coefficients for each of the three samples. For load step 9 of Sample
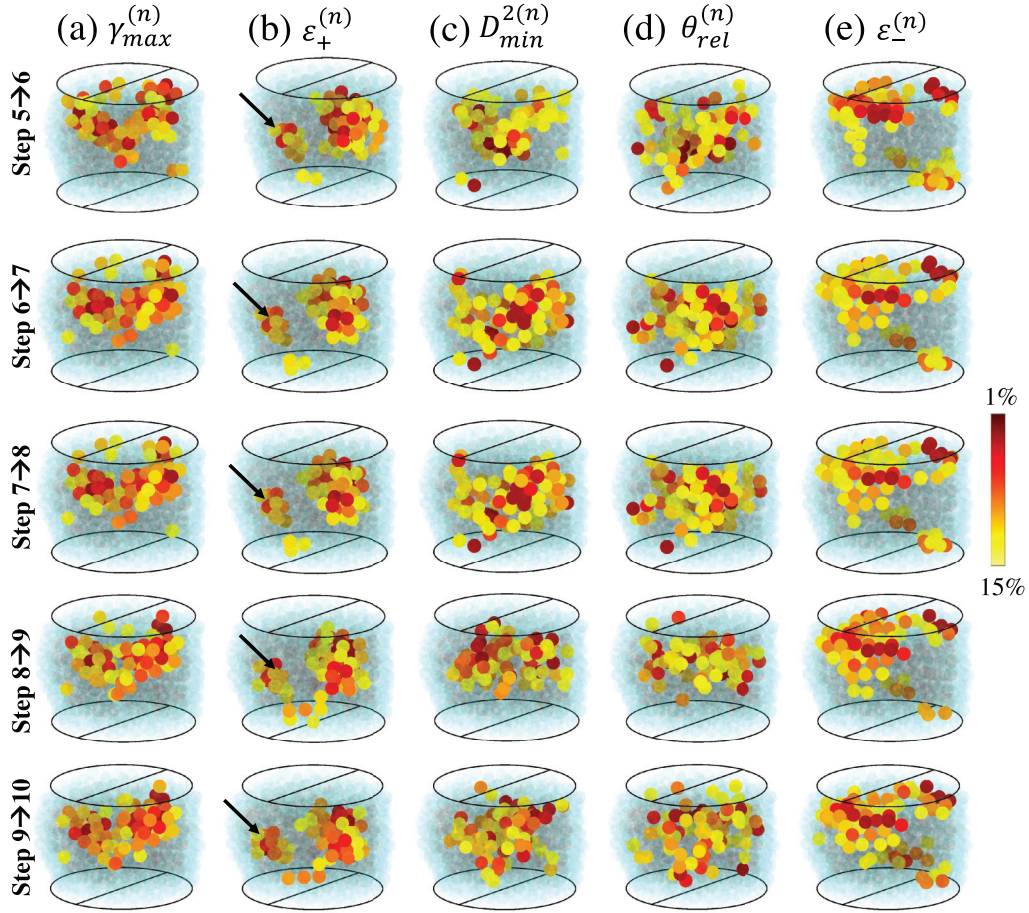
FIG. 5. Rendering of Sample B with particle-centered regions exhibiting the largest 15% of rearrangements (or most negative 15% for $\epsilon_-^{(n)}$) by magnitude for five load step increments. (a) $\gamma_{\max}^{(n)}$, (b) $\epsilon_+^{(n)}$, (c) $D_{\min}^{2(n)}$, (d) $\theta_{\mathrm{rel}}^{(n)}$, and (e) $\epsilon_-^{(n)}$. Colors indicate magnitude of normalized rearrangement from the largest (1%) to the smallest (15%) within the top 15%. Particles centered on local averaging regions for which rearrangements are calculated are rendered in translucent gray. Particles touching boundaries, included in calculations of local rearrangements but not featured at the center of local averaging regions, are rendered in translucent blue. Black arrows highlight regions that experience recurring rearrangements between distinct load step pairs or rearrangement events that span multiple load steps, as described in Sec. III F.

A, rearrangements appear correlated for $R_{sc} < 3r_p$, which is expected because local averaging regions used to calculate rearrangements around contacting particles ($R_{sc} \leqslant 2r_p$) overlap and thus share many similar terms in the sums in Eqs. (5), (7), and (9). For load step 9 of Sample A, rearrangement measures decay quickly for $R_{sc} > 3r_p$, suggesting that rearrangements separated by more than three particle radii do not share similar magnitudes. The decay is most pronounced for the rearrangements in the top 15% by magnitude. This pronounced decay can be also found for load step 3 of Sample C. For load step 8 of Sample B and load step 3 of Sample C, similar trends are observed for most rearrangements in the top 30% and 45% by magnitude. However, correlations are found to be weaker for $D_{\min}^{2(n)}$ and $\theta_{\mathrm{rel}}^{(n)}$ even for $R_{sc} < 3r_p$, suggesting that these rearrangement measures are highly localized in space to a greater degree than for Sample A. For all other load steps for Samples A, B, and C, correlations are either minimal even at $R_{sc} = 2r_p$ or decay rapidly above $R_{sc} = 3r_p$, as in Figs. 7(a), 7(b), and 7(c). We conclude from this analysis that a local averaging region of radius $r = 3r_p$ is sufficiently large to

capture local, isolated rearrangements that are not correlated over larger length scales.

D. Rearrangement correlations within regions

In the original STZ theory, STZ strains are oriented along the same principal axes as macroscopic stress, which constrains their shear and dilational strain coupling [14]. Here we examine the coupling between local shear and volumetric strain, $\gamma_{\max}^{(n)}$ and $\epsilon_\pm^{(n)}$, as well as other coocated pairs of rearrangement measures. We examine this coupling by calculating the correlation coefficient between rearrangements. In particular, we first-order rearrangements calculated between load steps s and $s + 1$ for a specific sample from largest (1%) to smallest (100%) for $\gamma_{\max}^{(n)}$, $\epsilon_+^{(n)}$, $D_{\min}^{2(n)}$, and $\theta_{\mathrm{rel}}^{(n)}$, and from most negative (1%) to most positive (100%) for $\epsilon_-^{(n)}$. We refer to these ordered rearrangements as $e(i, s, s + 1)^{(n)}$ or $g(i, s, s + 1)^{(n)}$, where e and g refer to distinct rearrangement measures. We then compute
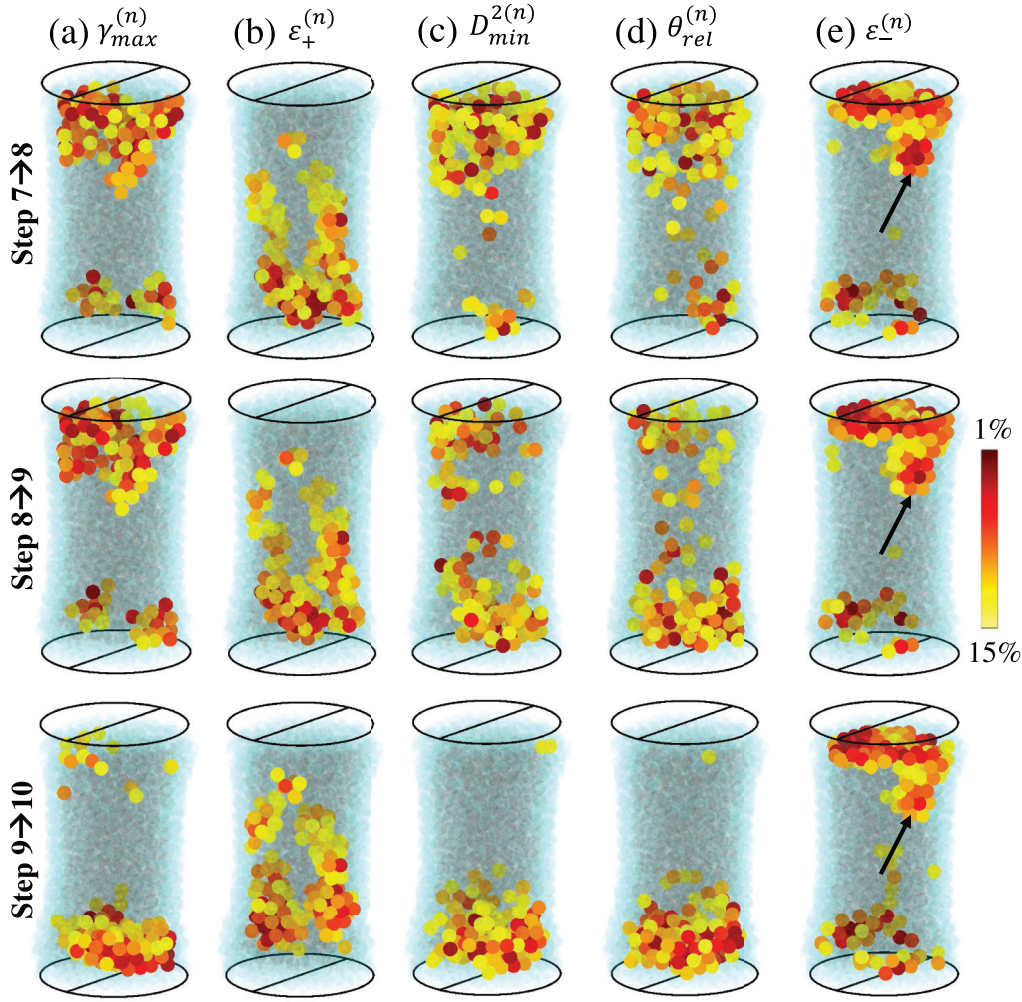
FIG. 6. Rendering of Sample C with particle-centered regions exhibiting the largest 15% of rearrangements (or most negative 15% for $\epsilon_-^{(n)}$) by magnitude for three load step increments. (a) $\gamma_{max}^{(n)}$, (b) $\epsilon_+^{(n)}$, (c) $D_{min}^{2(n)}$, (d) $\theta_{rel}^{(n)}$, and (e) $\epsilon_-^{(n)}$. Colors indicate magnitude of normalized rearrangement from the largest (1%) to the smallest (15%) within the top 15%. Particles centered on local averaging regions for which rearrangements are calculated are rendered in translucent gray. Particles touching boundaries, included in calculations of local rearrangements but not featured at the center of local averaging regions, are rendered in translucent blue. Black arrows highlight regions that experience recurring rearrangements between distinct load step pairs or rearrangement events that span multiple load steps, as described in Sec. III F.

$$\rho_e^g(s, s+1) = \frac{\sum_{i=1}^{N_\%}[e(i, s, s+1)^{(n)} - \langle e(s, s+1)^{(n)}\rangle][g(i, s, s+1)^{(n)} - \langle g(s, s+1)^{(n)}\rangle]}{\sqrt{\sum_{i=1}^{N_\%}[e(i, s, s+1)^{(n)} - \langle e(s, s+1)^{(n)}\rangle]^2}\sqrt{\sum_{i=1}^{N_\%}[g(i, s, s+1)^{(n)} - \langle g(s, s+1)^{(n)}\rangle]^2}}, \qquad (13)$$

where $N_\%$ is the number of rearrangements in the top $N\%$ as ordered by $e^{(n)}$. With $\rho_e^g(s, s+1)$ computed for each pair of consecutive load steps $(s, s+1)$ for all samples, we take an average to obtain the values shown in Fig. 8.

Figure 8 shows the average ρ_e^g across all samples and load steps. Some notable coupling between rearrangements can be observed. For instance, Fig. 8(a) orders regions within a sample and load step increment by magnitude of $\gamma_{max}^{(n)}$. The curve with circular symbols in Fig. 8(a) conveys the correlation between $\gamma_{max}^{(n)}$ and $\epsilon_{vol}^{(n)}$ in these regions. In other words, the local regions exhibiting the top 5% of $\gamma_{max}^{(n)}$ demonstrate a negative correlation (coefficient around -0.26) with volumetric strain,

$\epsilon_{vol}^{(n)}$; this is conveyed by the data point highlighted with an arrow in Fig. 8(a). This indicates that regions undergoing the largest shear strains tend to demonstrate volumetric contraction. On the other hand, correlations between $\gamma_{max}^{(n)}$ and $D_{min}^{(n)}$ or $\gamma_{max}^{(n)}$ and $\theta_{rel}^{(n)}$, represented by curves with square and upward triangular symbols, respectively, are small for regions undergoing the largest shear strains. As another example, Fig. 8(c) shows that regions exhibiting the largest 5% of $D_{min}^{2(n)}$ tend to feature correlations (coefficient around 0.2, black diamonds) between $D_{min}^{2(n)}$ and $\theta_{rel}^{(n)}$. This correlation grows as we examine the top $N > 5\%$ of rearrangements ordered by $D_{min}^{2(n)}$ in
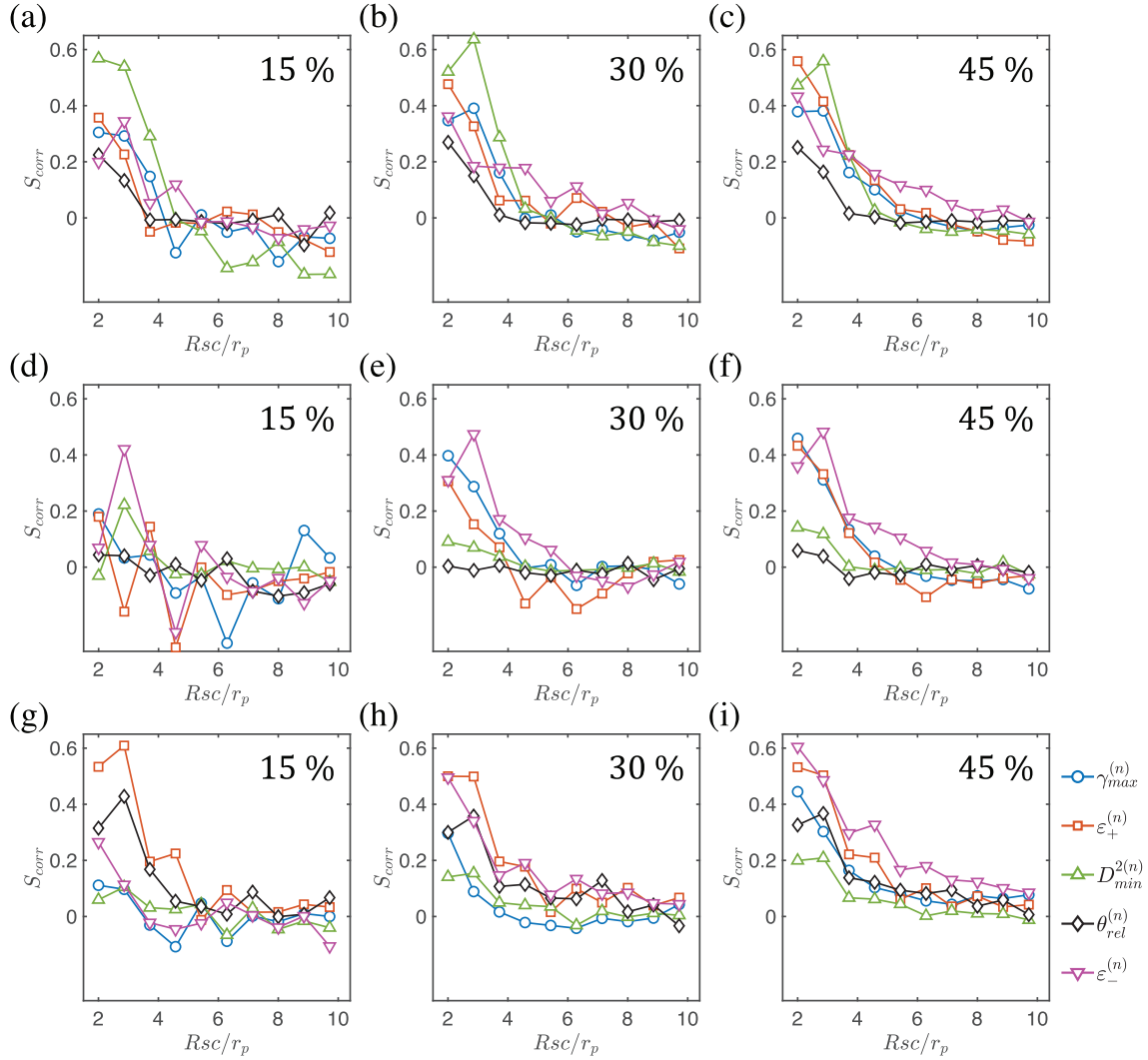
FIG. 7. Spatial correlation coefficient between rearrangements between load steps 9 and 10 of Sample A (top row), load steps 8 and 9 of Sample B (bottom row), and load steps 3 and 4 of Sample C (bottom row), as described in the text. In all cases, rearrangements are computed with $r = 3r_p$ and correlation coefficients are calculated using Eq. (12). Correlations are plotted as a function of the maximum distance between rearrangements, R_{sc}, and by considering only rearrangements within that maximum distance with the largest [(a), (d), (g)] 15%, [(b), (e), (h)] 30%, and [(c), (f), (i)] 45% of rearrangements by magnitude.

Fig. 8(c). As a final example, consider Fig. 8(e), which shows that regions exhibiting the largest volumetric contraction also exhibit strong correlations (coefficient around -0.37, blue circles) with shear strain.

To further examine rearrangement coupling and to distinguish features of this coupling that differ between samples, we next order regions within a given sample and load step increment by local strain $\epsilon_{zz}(i, s, s + 1)$ computed using Eq. (5) from most negative (1%) to most positive (100%). The sum of all such local strains for a sample and consecutive load step furnishes the macroscopic strain increment in Fig. 1(e),

$$\Delta\epsilon_{zz}^S(s, s + 1) \approx \frac{1}{V_r} \sum_{i=1}^{N_r} \epsilon_{zz}(i, s, s + 1)V_i, \qquad (14)$$

where N_r is all local regions for which rearrangements are calculated, V_i is the Voronoi cell volume around a particle in

region i, V_r is the sum of the N_r volumes V_i, and "$\approx$" reflects the slight deviation of the sum from the global strain because particles contacting boundaries are not considered as local regions for which rearrangements are calculated [44]. We again obtain the correlations shown in Fig. 9 by using Eq. (13) with these ordered regions. Unlike in Fig. 8, we do not average over all samples but only over all load step increments within samples. We observe significant differences between samples and also higher correlation coefficients than when samples were analyzed together in Fig. 8. In particular, while correlations between rearrangements ordered by strains in Fig. 9 do not exceed 0.3 in Sample A, we observe correlations between 0.25 and as high as 0.55 between $D_{\min}^{2(n)}$ and $\theta_{\rm rel}^{(n)}$, $\gamma_{\max}^{(n)}$ and $\theta_{\rm rel}^{(n)}$, and $\gamma_{\max}^{(n)}$ and $D_{\min}^{2(n)}$ in Samples B and C for regions with the most negative $\epsilon_{zz}(i)$. This suggests that regions contributing the most to the macroscopic compaction in Samples B and C feature correlations between nonaffine displacement and
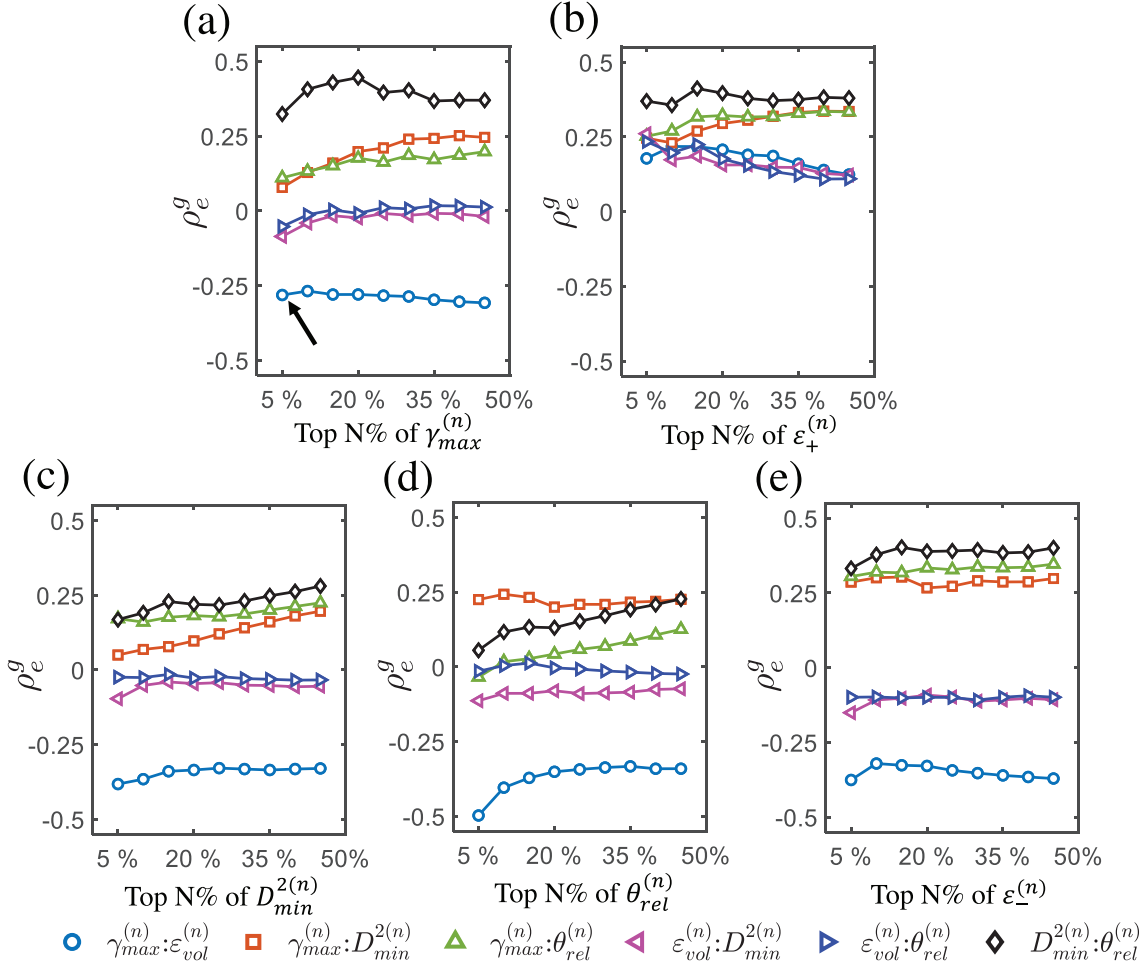
FIG. 8. Correlation coefficients between colocated rearrangements in the top $N\%$ of all rearrangements for a specific load step, averaging over all samples and load step pairs, as ordered by (a) $\gamma_{max}^{(n)}$, (b) $\epsilon_+^{n)}$, (c) $D_{min}^{2(n)}$, (d) $\theta_{rel}^{(n)}$, and $\epsilon_-^{(n)}$. In each case the symbols in the legend correspond to the e and g used in Eq. (13).
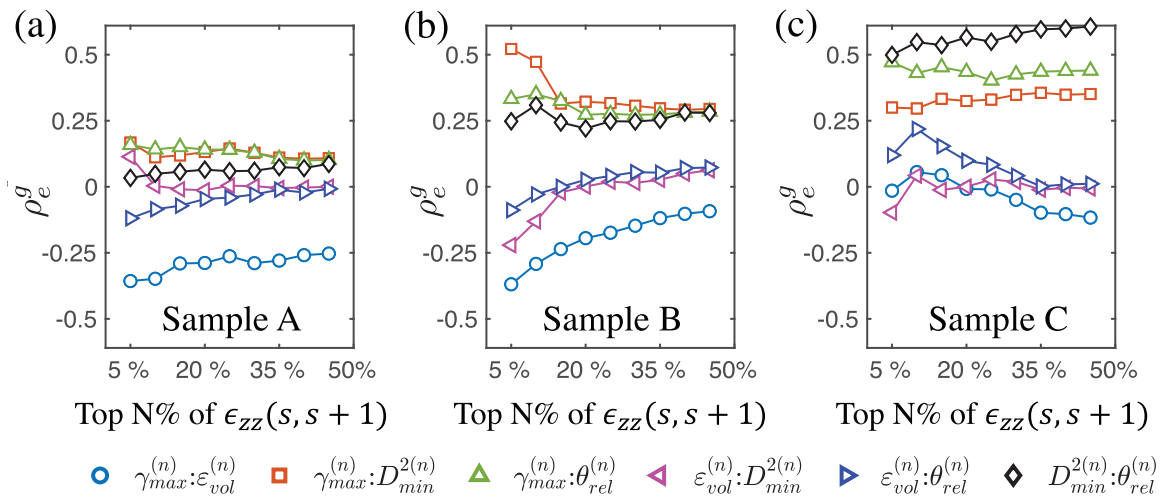

FIG. 9. Average correlation coefficients between colocated local strains $\epsilon_{zz}(i)$ in the top $N\%$ (from greatest to least) and local rearrangements between consecutive load steps for (a) Sample A, (b) Sample B, and (c) Sample C. In each case the symbols in the legend correspond to the e and g used in Eq. (13).

relative rotation, and nonaffine displacement or relative rotation and shear strain.

In summary, our most notable findings from this subsection are that regions exhibiting the largest (by magnitude) shear strains tend to exhibit non-negligible correlations with the large dilatational or contractile strains, and regions exhibiting the largest dilatational or contractile strains (by magnitude) tend to exhibit non-negligible correlations with the large shear strains. Similarly, regions exhibiting the largest $D_{\min}^{2(n)}$ tend to exhibit non-negligible correlations with the large $\theta_{\text{rel}}^{(n)}$. Furthermore, regions contributing the most to the macroscopic sample compaction tend to exhibit coupling between nonaffine motion or relative rotation and shear strain, particularly for Samples B and C.

Despite our observations, the distinct locations of rearrangements in Figs. 4–6, and the fact that ρ_e^g remains below 0.55 in Figs. 8 and 9 suggests that although rearrangement measures are correlated, they provide distinct information about behavior in local averaging regions. It is most clear from Figs. 4–6 that extreme values of rearrangement measures, such as $\theta_{\text{rel}}^{(n)}$, are able to isolate regions of local deformation that are not isolated by examining extreme values of $D_{\min}^{2(n)}$ or $\epsilon_{-}^{(n)}$, and vice versa. To supplement our investigation of rearrangement coupling in Fig. 9, we next investigate how regions identified by the largest values of each rearrangement measure contribute to the macroscopic sample compaction.

E. Contributions of rearranging regions to macroscopic sample strain

Measures such as $D_{\min}^{2(n)}$ are frequently and effectively used to identify regions of a material experiencing more nonaffine motion than surrounding neighborhoods [14,16,43]. It is not clear, however, how significantly regions with elevated $D_{\min}^{2(n)}$ magnitudes, or elevated magnitudes of other rearrangement measures, contribute to macroscopic strain of materials under various boundary conditions. In the idealized form of the original STZ theory, STZs should account for all of the inelastic deformation of a solid undergoing pure shear [14]. Quantitative contributions of STZs to inelastic deformation in various geometries and for various boundary conditions therefore deserves further study.

Here we examine the contribution of local regions exhibiting specific rearrangements to the macroscopic sample strain increment. In particular, we first order rearrangements calculated between load steps s and $s + 1$ by magnitude, from largest (1%) to smallest (100%) for $\gamma_{\max}^{(n)}$, $\epsilon_{+}^{(n)}$, $D_{\min}^{2(n)}$, and $\theta_{\text{rel}}^{(n)}$, and from most negative (1%) to most positive (100%) for $\epsilon_{-}^{(n)}$. We then select regions exhibiting the largest (or most negative for $\epsilon_{-}^{(n)}$) $N\%$ to $(N + 10)\%$ of rearrangements for each load step increment, where N varies from 0 to 90 in increments of 10. Let there be N_{rr} such regions for a given load step increment and let $\Delta\epsilon_{zz}^S(s, s + 1)$ denote the sample strain between those steps, s and $s + 1$. The fractional contribution of these regions to the sample strain increment is given by

$$\nu(e, s, s + 1, N\%) \approx \frac{\frac{1}{V_{rr}}\sum_{i=1}^{N_{rr}}\epsilon_{zz}(i, s, s + 1)V_i}{\Delta\epsilon_{zz}^S(s, s + 1)}, \qquad (15)$$

where $\epsilon_{zz}(i, s, s + 1)$ is the particle-centered strain tensor component zz at the center of region i computed from Eq. (5), V_i is the rearrangement volume $[4/3\pi(3r_p)^3]$, V_{rr} is the sum of the N_{rr} volumes V_i. If all regions exhibit the same strain (i.e., the deformation is affine or uniform), then $\nu(e, s, s + 1, N\%) = 0.1$ for each value of $N\%$ in Eq. (15). If, on the other hand, all macroscopic strain between s and $s + 1$ is furnished by the top 10% of rearrangements, $\nu(e, s, s + 1, 0\%) = 1.0$ and $\nu(e, s, s + 1, N\%) = 0.0$ for all $N \neq 0$.

Figure 10 shows the result of Eq. (15) as a percentage ($\nu \times 100\%$). From the leftmost column of Fig. 10, we observe that regions experiencing the largest 10% of shear strain between consecutive load steps contribute between 15% and 25% of the incremental macroscopic sample strain, depending on the specific sample and load step. Similar trends are observed in the three rightmost columns of Fig. 10 for rearrangements ordered by $D_{\min}^{2(n)}$, $\theta_{\text{rel}}^{(n)}$, and $\epsilon_{-}^{(n)}$, but to a lesser extent, surprisingly even for $\epsilon_{-}^{(n)}$. The second column in Fig. 10 shows that, as expected, regions experiencing the largest $\epsilon_{+}^{(n)}$ contribute the least to incremental macroscopic sample strain. This is expected because samples undergo macroscopic compaction in all cases considered here, which are not accommodated at all by $\epsilon_{+}^{(n)}$.

We interpret the results of our calculations in this subsection to suggest that local regions exhibiting the largest shear strain, $\gamma_{\max}^{(n)}$, are those that also contribute most significantly to the macroscopic sample compaction, at least for the geometries and boundary conditions considered in this paper. Regions exhibiting the largest values of $D_{\min}^{2(n)}$ also contribute more to macroscopic sample strain than expected from an affine deformation, but do not contribute as significantly as regions exhibiting the largest shear strains. This finding supports our approach of evaluating multiple measures of local rearrangements, each of which contributes in a different manner to the macroscopic strain.

F. Rearrangement repeatability

An important question is whether rearrangements events can occur repeatedly in a single local region, or whether, once a rearrangement occurs in a local region, that region can no longer undergo a rearrangement event. This question is central to ideas in STZ theory and elastoplastic models; in the latter, it is hypothesized that local plastic events lead to a complete relaxation of the local stress [41], thus requiring further strain or significant activation from nearby plastic events to recur in the same location. Our measurements allow us to study the repeatability of rearrangements in local regions; however, as we will show by the end of this subsection, we do not have the ability distinguish between events that recur in the same regions and events that span multiple macroscopic strain increments. In contrast, in simulations one may examine the cascade of avalanches by examining progressively finer time intervals (e.g., [14,43]).

To compute the repeatability of rearrangements, we calculate the autocorrelation of rearrangement magnitude in every region between steps s and $s + 1$ (called $s1$) with rearrangement magnitude in the same region (i.e., having the same
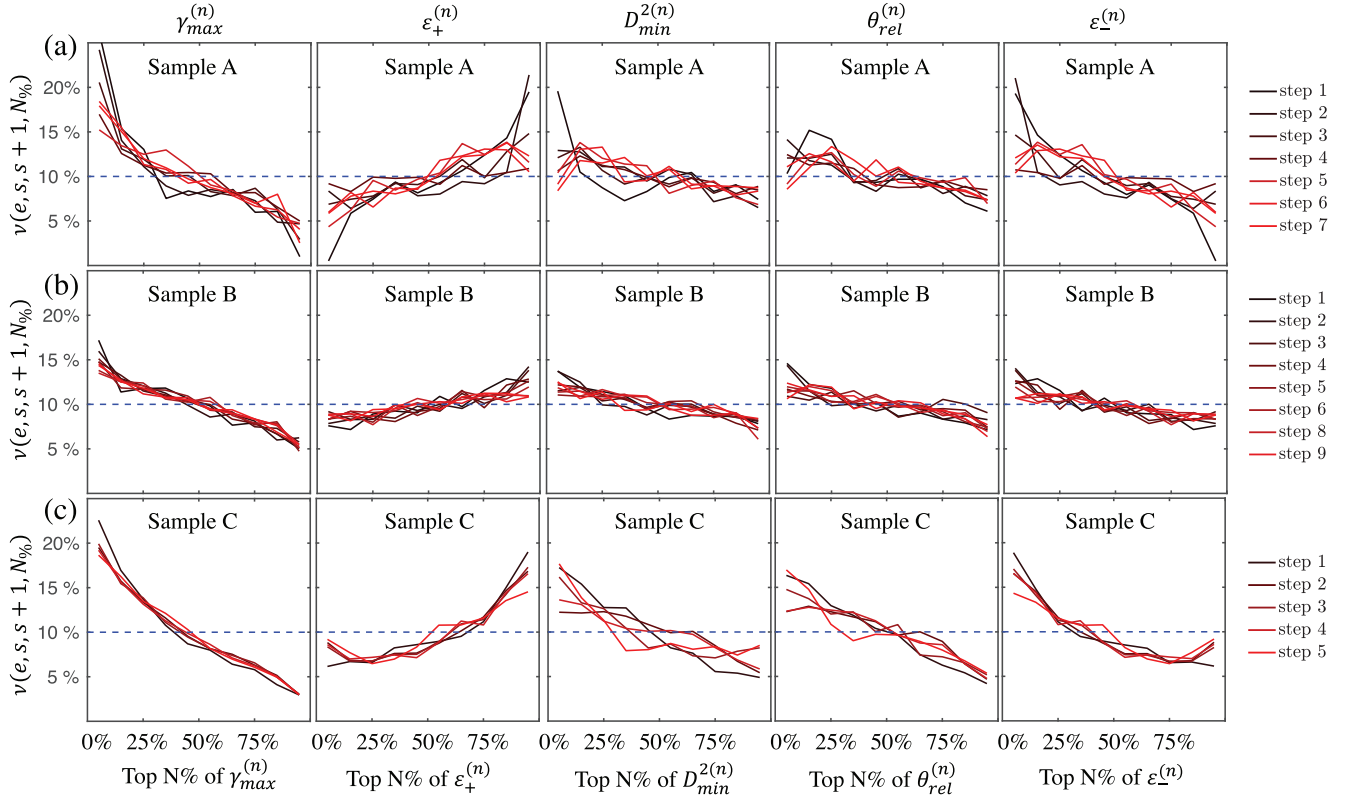
FIG. 10. Fractional contribution of regions exhibiting the top $N\%$ to $(N + 10)\%$ of rearrangements [or the most negative $N\%$ to most negative $(N + 10)\%$ in the case of $\epsilon_-^{(n)}$] to the macroscopic sample strain, as calculated by Eq. (15) and described in the text. Each curve represents rearrangements calculated between steps s and $s + 1$. Curves are labeled by step s in each row. The dashed blue curve represents the expected distribution in the scenario in which regions featuring rearrangements of all sizes contribute equally to the macroscopic strain.

central particle) between steps $s - 1$ and s (called $s2$). We also repeat this calculation for rearrangement magnitudes between

steps s and $s + 1$ and those between $s - 2$ and $s - 1$ and $s - 3$ and $s - 2$ (also called $s2$). The calculation is performed by

$$\rho_{e(s1)}^{e(s2)} = \frac{\sum_{i=1}^{N_r}[e(i, s1)^{(n)} - \langle e(s1)^{(n)}\rangle][e(i, s2)^{(n)} - \langle e(s2)^{(n)}\rangle]}{\sqrt{\sum_{i=1}^{N_r}[e(i, s1)^{(n)} - \langle e(s1)^{(n)}\rangle]^2}\sqrt{\sum_{i=1}^{N_r}[e(i, s2)^{(n)} - \langle e(s2)^{(n)}\rangle]^2}},$$ (16)

where $e(i)^{(n)}$ is a normalized rearrangement around particle i and N_r is all such rearrangements considered for a given sample and load step. Figure 11(a) shows the result of this calculation as a function of the increment in sample strain between the first load step of $s2$ and $s1$. Figure 11(b) shows the result of the calculation as a function of the hydrostatic sample stress at the first load step of $s1$. Dashed lines are least-squares fits between the correlation coefficients computed for all possible pairs $s1$ and $s2$ and $\Delta\epsilon_{zz}^S$ [Fig. 11(a)] or σ_h^V [Fig. 11(b)].

In Fig. 11(a) we observe that strain-based rearrangements ($\gamma_{\max}^{(n)}$, $\epsilon_+^{(n)}$, and $\epsilon_-^{(n)}$) either recur in a region when incremental strains are close to zero, or occur over multiple sample strain increments. These two scenarios are not distinguishable from our data. As sample strain increases between the first step of the two strain increments from which rearrangements are calculated, the autocorrelation decreases for all rearrangement measures. The measures $D_{\min}^{2(n)}$ and $\theta_{\mathrm{rel}}^{(n)}$ do not possess a correlation greater than about 0.3, suggesting that they are either

less likely to recur in a region or occur over smaller sample strain increments. Further correlation analysis of $\rho_{e(s1)}^{e(s2)}$ with $\Delta\epsilon_{zz}^S$ in Fig. 11(a) is carried out for each rearrangement measure e and yields correlation coefficients of 0.47, 0.52, 0.41, 0.36, and 0.38 for $\gamma_{\max}^{(n)}$, $\epsilon_+^{(n)}$, $D_{\min}^{2(n)}$, $\theta_{\mathrm{rel}}^{(n)}$, and $\epsilon_-^{(n)}$, respectively, all with p values less than 10^{-4}. Correlation analysis of $\rho_{e(s1)}^{e(s2)}$ with σ_h^V yields coefficients of -0.47, -0.55, -0.06, 0.06, and -0.52 for $\gamma_{\max}^{(n)}$, $\epsilon_+^{(n)}$, $D_{\min}^{2(n)}$, $\theta_{\mathrm{rel}}^{(n)}$, and $\epsilon_-^{(n)}$, respectively, all with p values less than 10^{-4}.

In Fig. 11(b) we observe that strain-based rearrangements ($\gamma_{\max}^{(n)}$, $\epsilon_+^{(n)}$, and $\epsilon_-^{(n)}$) either recur in a region when hydrostatic sample stress is high, or occur over large sample strain increments. Again, these two scenarios are not distinguishable from our data. The autocorrelation again decreases for all rearrangement measures as sample stress decreases. Again, the measures $D_{\min}^{2(n)}$ and $\theta_{\mathrm{rel}}^{(n)}$ have lower fitted correlation coefficients (dashed lines), below about 0.2, suggesting they are not highly dependent on σ_h^V.
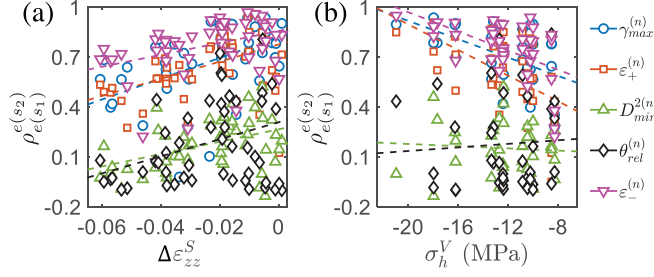
FIG. 11. Autocorrelation between rearrangement magnitudes calculated between load step pairs $s1$ and $s2$ using Eq. (16), as explained in the main text, plotted as a function of (a) $\Delta \epsilon_{zz}^{S}$ between the first load step of pairs $s1$ and $s2$ and (b) σ_h^V in the first step of $s1$.

The question of whether a rearrangement event relaxes local stress and rearrangements local structure in a manner that reduces the likelihood of subsequent rearrangements in that neighborhood is critical for the construction of elastoplastic theories of flow (e.g., [41]). We conclude that we do not have sufficient detail from our measurements to provide a definitive answer to this question, but our results suggest that local rearrangements may recur in the same local regions over small strain increments or occur over multiple strain increments, at least in the geometries and for the boundary conditions studied here. This conclusion is further supported by visual analysis of the rearrangements provided in Fig. 4–6 and discussed in Sec. III C.

G. Dependence of rearrangements on stresses and structure

A striking finding from recent research on rearrangements in amorphous and granular materials is that the location and magnitude of rearrangements may be predicted accurately with only measures of local structure [4,8,45]. Here we show that for Samples A and B, we observe only a weak dependence of local rearrangement on local stress prior to rearrangement and a stronger dependence on local structure; however, we stop short of performing any machine learning for "softness," as was done in [45].

We compute the correlation of the stress in a region with the magnitude of a rearrangement event by first ordering rearrangements for a specific sample and load step increment s to $s+1$ by magnitude, from largest (1%) to smallest (100%) for $\gamma_{max}^{(n)}$, $\epsilon_+^{(n)}$, $D_{min}^{2(n)}$, and $\theta_{rel}^{(n)}$, and from most negative (1%) to most positive (100%) for $\epsilon_-^{(n)}$. Within the regions corresponding to the largest $N\%$ rearrangements, we then consider three measures, σ, of the local stress in the region at load step s: the hydrostatic stress, $\sigma_h^{(n)}$, the angle between the maximum shear stress and strain directions, $\theta_{\gamma_{max}}^{\tau_{max(n)}}$, and the maximum shear stress, $\tau_{max}^{(n)}$. For $\theta_{\gamma_{max}}^{\tau_{max(n)}}$, γ_{max} is computed between steps $s-1$ and s. Like the rearrangements, the stress measures are also normalized in each sample and load step by subtracting their mean and dividing by their standard deviation, as in Eq. (11) for e. We compute the correlation between the stress measure σ at step s with the rearrangement magnitude between s and $s+1$ by

$$\rho_{\sigma(s)}^{e(s,s+1)} = \frac{\sum_{i=1}^{N_\%}[e(i,s,s+1)^{(n)} - \langle e(s,s+1)^{(n)} \rangle][\sigma(i,s)^{(n)} - \langle \sigma(s)^{(n)} \rangle]}{\sqrt{\sum_{i=1}^{N_\%}[e(i,s,s+1)^{(n)} - \langle e(s,s+1)^{(n)} \rangle]^2}\sqrt{\sum_{i=1}^{N_\%}[\sigma(i,s)^{(n)} - \langle \sigma(s)^{(n)} \rangle]^2}}, \tag{17}$$

where $N_\%$ is the number of rearrangements in the top $N\%$ as ordered by magnitude of rearrangement measure $e(s,s+1)^{(n)}$. Figure 12 shows the correlation coefficients calculated using Eq. (17). The striking finding from this figure is that stress immediately prior to rearrangements it not noticeably correlated with rearrangement magnitude as measured by any of the five rearrangements we consider here. On the other hand, we repeated the calculation of Eq. (17) but by replacing stress measures σ by local porosity in an averaging region, ϕ, which is calculated by the total volume of voids (volume minus grain volume) in the region divided by the total volume of the region. The resulting correlations, $\rho_{\phi(s)}^{e(s,s+1)}$, are shown in Fig. 13.

Unlike in Fig. 12, in Fig. 13 we observe moderate correlations between local porosity in a region in step s and rearrangement between steps s and $s+1$. The correlations coefficients range from 0.2 to 0.3 for the largest values of $D_{min}^{2(n)}$ and $\epsilon_+^{(n)}$ for Samples A and C, are around 0.2 for $D_{min}^{2(n)}$ for Sample B. Other rearrangements feature lower correlation coefficients with porosity immediately prior to rearrangements.

IV. DISCUSSION AND CONCLUSIONS

We systematically studied local rearrangements in three samples of deforming 3D granular materials by using *in situ* x-ray measurements of particle positions and stresses. We defined five distinct rearrangement measures and examined their statistics, interrelationships, contributions to macroscopic deformation, repeatability, and dependence on local structure and stress. The most significant findings of our study are that (1) local rearrangements are correlated at a scale of about three to four particle diameters, (2) rearrangements exhibit volumetric strain-shear strain and nonaffine displacement-rotation coupling, (3) rearrangements exhibit correlations that suggest either memory effects (i.e., rearrangements can occur in the same location twice) or that individual rearrangement events may occur over multiple increments of sample strain, and (4) rearrangements show little dependence on local stress but correlate with quantities describing local structure.

The finding that rearrangements are correlated at a scale of three to four particle diameters is consistent with prior work in metallic glasses [14], colloidal glasses [5], and granular materials [8]; however, while prior studies primarily examined
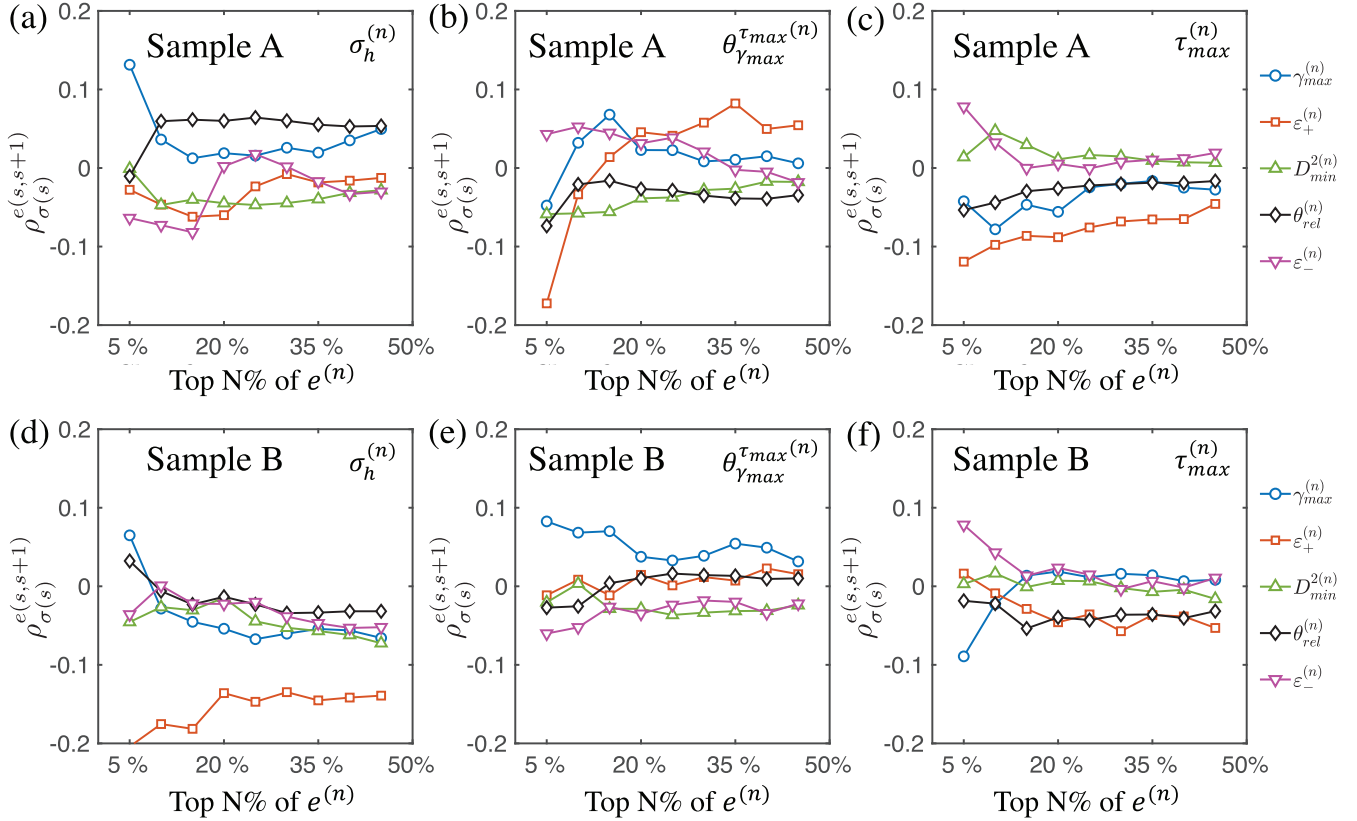
FIG. 12. Correlation between local stress measures at load step s, $\sigma(s)$ and local rearrangements between load steps s and $s+1$, as calculated by Eq. (17) and described in the text. The top row shows results for Sample A, and the bottom row shows results for Sample B. Stress measures are (a, d) hydrostatic sample stress, $\sigma_h^{(n)}$, (b, e) the angle between the maximum shear strain and stress directions, $\theta_{\gamma max}^{\tau_{\max}(n)}$, and (c, f) the maximum shear stress, $\tau_{\max}^{(n)}$. In all cases, rearrangements are considered only in the top $N\%$, as ordered from largest (1%) to smallest (100%) for $\gamma_{\max}^{(n)}$, $\epsilon_+^{(n)}$, $D_{\min}^{2(n)}$, and $\theta_{\mathrm{rel}}^{(n)}$ and from most negative (1%) to most positive (100%) for $\epsilon_-^{(n)}$.

macroscopic pure or simple shear, we have shown here that this finding also holds for confined geometries in uniaxial, hydrostatic, and triaxial compression (Samples A, B, and C, respectively).

The coupling between volumetric and shear strain of individual regions experiencing rearrangements is related to assumptions of STZ theories [14] and deserves further study in other loading geometries. Our analysis suggests that al-

though such a coupling exists, there is a broad distribution of event types with no single event being "typical," as reflected by the low correlation coefficients in Figs. 8 and 9 and discussed in Sec. III D.

Our analysis suggests that rearrangements, as measured by local strain ($\gamma_{\max}^{(n)}$, $\epsilon_+^{(n)}$, and $\epsilon_-^{(n)}$), either can recur in the same location twice or can occur over multiple quasistatic strain increments. Rearrangements measured by $D_{\min}^{2(n)}$ or $\theta_{\mathrm{rel}}^{(n)}$ appear
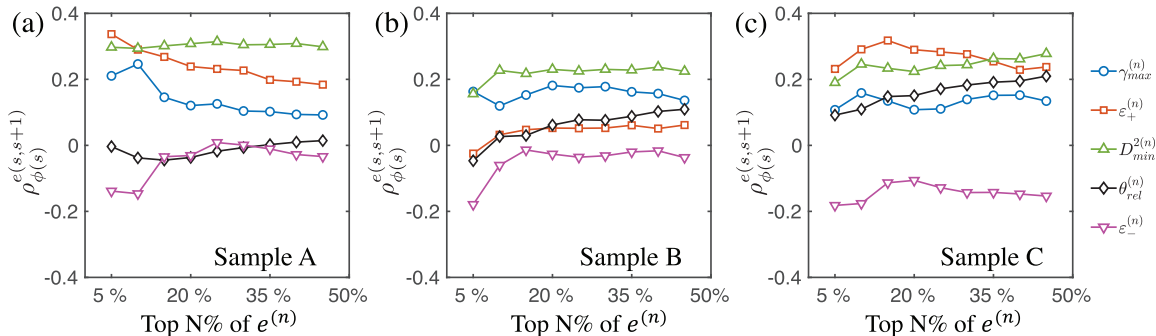

FIG. 13. Correlation between local porosity at load step s, $\phi(s)$ and local rearrangements between load steps s and $s+1$, as calculated by Eq. (17) and described in the text. Results are averaged for all consecutive load steps of (a) Sample A, (b) Sample B, and (c) Sample C. In all cases, rearrangements are considered only in the top $N\%$, as ordered from largest (1%) to smallest (100%) for $\gamma_{\max}^{(n)}$, $\epsilon_+^{(n)}$, $D_{\min}^{2(n)}$, and $\theta_{\mathrm{rel}}^{(n)}$ and from most negative (1%) to most positive (100%) for $\epsilon_-^{(n)}$.

to be more localized in sample strain and are less likely to occur over multiple quasistatic strain increments. This finding supports the notion that our five rearrangement measures offer distinct views of the nature of local deformation accommodating macroscopic strain. We save for future work the study of whether individual rearrangements are reversible under reversals of strain or repeatable under strain cycles at certain strain magnitudes, which may provide further insight into strains required for retention of "memory" and transitions to "chaotic" behavior (e.g., see [46–48]).

Finally, our analysis suggests that no single stress or local structure measure is significantly correlated to rearrangement magnitude, although local porosity did appear to correlate more highly than local hydrostatic or shear stress. This finding may reflect resolution limitations of stress measurements by 3DXRD, but may also suggest a more complex set of structure indicators is needed to predict rearrangement location and magnitude. The latter idea is aligned with recent work showing that local structure indicators like "softness," a machine-learned function of pair-correlation functions, or steric bond order do provide very accurate predictions of local rearrangement location and magnitude [4,8,45]. We save application of those tools to our data for future work.

We conclude here by noting that our measurements provide a unique, experimental view of local rearrangements in 3D granular materials in various geometries and under various loading conditions. Our results highlight the various roles of local rearrangements and their coupling in furnishing macroscopic strain. Our findings also contribute to the ongoing search for a combination of structural defects and stress states that promote local rearrangements in granular and amorphous materials.

[1] A. Le Bouil, A. Amon, S. McNamara, and J. Crassous, Emergence of Cooperativity in Plasticity of Soft Glassy Materials, Phys. Rev. Lett. **112**, 246001 (2014).

[2] A. Baule, F. Morone, H. J. Herrmann, and H. A. Makse, Edwards statistical mechanics for jammed granular matter, Rev. Mod. Phys. **90**, 015006 (2018).

[3] D. Bonn, M. M. Denn, L. Berthier, T. Divoux, and S. Manneville, Yield stress materials in soft condensed matter, Rev. Mod. Phys. **89**, 035005 (2017).

[4] E. D. Cubuk, R. Ivancic, S. S. Schoenholz, D. Strickland, A. Basu, Z. Davidson, J. Fontaine, J. L. Hor, Y.-R. Huang, Y. Jiang *et al.*, Structure-property relationships from universal signatures of plasticity in disordered solids, Science **358**, 1033 (2017).

[5] P. Schall, D. A. Weitz, and F. Spaepen, Structural rearrangements that govern flow in colloidal glasses, Science **318**, 1895 (2007).

[6] L. Bécu, S. Manneville, and A. Colin, Yielding and Flow in Adhesive and Nonadhesive Concentrated Emulsions, Phys. Rev. Lett. **96**, 138302 (2006).

[7] M. L. Manning and A. J. Liu, Vibrational Modes Identify Soft Spots in a Sheared Disordered Packing, Phys. Rev. Lett. **107**, 108302 (2011).

[8] E. D. Cubuk, S. S. Schoenholz, J. M. Rieser, B. D. Malone, J. Rottler, D. J. Durian, E. Kaxiras, and A. J. Liu, Identifying Structural Flow Defects in Disordered Solids using Machine-Learning Methods, Phys. Rev. Lett. **114**, 108001 (2015).

[9] X. Yang, R. Liu, M. Yang, W.-H. Wang, and K. Chen, Structures of Local Rearrangements in Soft Colloidal Glasses, Phys. Rev. Lett. **116**, 238003 (2016).

[10] J. Zylberg, E. Lerner, Y. Bar-Sinai, and E. Bouchbinder, Local thermal energy as a structural indicator in glasses, Proc. Natl. Acad. Sci. USA **114**, 7289 (2017).

[11] B. Xu, M. L. Falk, J. F. Li, and L. T. Kong, Predicting Shear Transformation Events in Metallic Glasses, Phys. Rev. Lett. **120**, 125503 (2018).

[12] C. L. Kelchner, S. J. Plimpton, and J. C. Hamilton, Dislocation nucleation and defect structure during surface indentation, Phys. Rev. B **58**, 11085 (1998).

[13] A. Argon and H. Kuo, Plastic flow in a disordered bubble raft (an analog of a metallic glass), Mater. Sci. Eng. **39**, 101 (1979).

[14] M. L. Falk and J. S. Langer, Dynamics of viscoplastic deformation in amorphous solids, Phys. Rev. E **57**, 7192 (1998).

[15] P. Sollich, F. Lequeux, P. Hébraud, and M. E. Cates, Rheology of Soft Glassy Materials, Phys. Rev. Lett. **78**, 2020 (1997).

[16] D. Chen, D. Semwogerere, J. Sato, V. Breedveld, and E. R. Weeks, Microscopic structural relaxation in a sheared supercooled colloidal liquid, Phys. Rev. E **81**, 011403 (2010).

[17] D. M. Mueth, G. F. Debregeas, G. S. Karczmar, P. J. Eng, S. R. Nagel, and H. M. Jaeger, Signatures of granular microstructure in dense shear flows, Nature (London) **406**, 385 (2000).

[18] M. R. Kuhn and K. Bagi, Contact rolling and deformation in granular media, Int. J. Solids Struct. **41**, 5793 (2004).

[19] A. Peshkov, M. Girvan, D. C. Richardson, and W. Losert, Reversibility of granular rotations and translations, Phys. Rev. E **100**, 042905 (2019).

[20] W. Losert, K. Ronaszegi, J. Weijs, J. A. Dijksman, and S. Slotterback, Three dimensional particle rearrangements during slow granular shear flow in a split bottom geometry, in *Powder*

and Grains 2009: Proceeding on the 6th International Conference on Micromechanics of Granular Media, edited by M. Nakagawa and S. Luding, AIP Conf. Proc. No. 1145 (American Institute of Physics, New York, 2009), pp. 347–350.

[21] M. Saadatfar, H. Takeuchi, V. Robins, N. Francois, and Y. Hiraoka, Pore configuration landscape of granular crystallization, Nat. Commun. **8**, 15082 (2017).

[22] N. Francois, M. Saadatfar, R. Cruikshank, and A. Sheppard, Geometrical Frustration in Amorphous and Partially Crystallized Packings of Spheres, Phys. Rev. Lett. **111**, 148001 (2013).

[23] J.-C. Tsai, G. A. Voth, and J. P. Gollub, Internal Granular Dynamics, Shear-Induced Crystallization, and Compaction Steps, Phys. Rev. Lett. **91**, 064301 (2003).

[24] A. Amon, V. B. Nguyen, A. Bruand, J. Crassous, and E. Clément, Hot Spots in an Athermal System, Phys. Rev. Lett. **108**, 135502 (2012).

[25] E. D. Cubuk, S. S. Schoenholz, E. Kaxiras, and A. J. Liu, Structural properties of defects in glassy liquids, J. Phys. Chem. B **120**, 6139 (2016).

[26] T. A. Sharp, S. L. Thomas, E. D. Cubuk, S. S. Schoenholz, D. J. Srolovitz, and A. J. Liu, Machine learning determination of atomic dynamics at grain boundaries, Proc. Natl. Acad. Sci. USA **115**, 10943 (2018).

[27] D. M. Sussman, S. S. Schoenholz, E. D. Cubuk, and A. J. Liu, Disconnecting structure and dynamics in glassy thin films, Proc. Natl. Acad. Sci. USA **114**, 10601 (2017).

[28] M. Harrington, A. J. Liu, and D. J. Durian, Machine learning characterization of structural defects in amorphous packings of dimers and ellipses, Phys. Rev. E **99**, 022903 (2019).

[29] R. C. Hurley, S. A. Hall, J. E. Andrade, and J. Wright, Quantifying Interparticle Forces and Heterogeneity in 3D Granular Materials, Phys. Rev. Lett. **117**, 098005 (2016).

[30] J. Oddershede, S. Schmidt, H. F. Poulsen, H. O. Sørensen, J. Wright, and W. Reimers, Determining grain resolved stresses in polycrystalline materials using three-dimensional x-ray diffraction, J. Appl. Crystallogr. **43**, 539 (2010).

[31] C. Zhai, E. Herbold, S. Hall, and R. Hurley, Particle rotations and energy dissipation during mechanical compression of granular materials, J. Mech. Phys. Solids **129**, 19 (2019).

[32] A. Mirone, E. Brun, E. Gouillart, P. Tafforeau, and J. Kieffer, The PyHST2 hybrid distributed code for high speed tomographic reconstruction with iterative reconstruction and a priori knowledge capabilities, Nucl. Instrum. Methods Phys. Res., Sect. B **324**, 41 (2014).

[33] J. Wright, Imaged11, https://github.com/FABLE-3DXRD/ImageD11 (2020).

[34] R. C. Hurley, E. B. Herbold, and D. C. Pagan, Characterization of the crystal structure, kinematics, stresses and rotations in angular granular quartz during compaction, J. Appl. Crystallogr. **51**, 1021 (2018).

[35] R. C. Hurley, *Stress and force measurement uncertainties in 3D granular materials, in EPJ Web of Conferences*, Vol. 249 (EDP Sciences, 2021), p. 02009.

[36] E. Ando, Experimental investigation of microstructural changes in deforming granular media using x-ray tomography, Ph.D. thesis, Université de Grenoble (2013).

[37] C. Rycroft, Voro++: A three-dimensional Voronoi cell library in C + +, https://www.osti.gov/biblio/946741 (2009).

[38] R. Hurley, S. Hall, and J. Wright, Multi-scale mechanics of granular solids from grain-resolved x-ray measurements, Proc. R. Soc. A **473**, 20170491 (2017).

[39] K. Bagi, Stress and strain in granular assemblies, Mech. Mater. **22**, 165 (1996).

[40] See Supplemental Material at http://link.aps.org/supplemental/10.1103/PhysRevE.105.014904 for the particle positions and contact positions and orientations for all samples, as well as the particle stress tensors and forces for Samples A and B..

[41] L. Bocquet, A. Colin, and A. Ajdari, Kinetic Theory of Plastic Flow in Soft Glassy Materials, Phys. Rev. Lett. **103**, 036001 (2009).

[42] E. W. Weisstein, Sphere-sphere intersection, https://mathworld.wolfram.com/ (2007).

[43] E. Stanifer and M. L. Manning, Avalanche dynamics in sheared athermal particle packings occurs via localized bursts predicted by unstable linear response, arXiv:2110.02803 (2021).

[44] R. C. Hurley, J. Lind, D. C. Pagan, M. A. Homel, M. C. Akin, and E. B. Herbold, Linking initial microstructure and local response during quasistatic granular compaction, Phys. Rev. E **96**, 012905 (2017).

[45] S. S. Schoenholz, E. D. Cubuk, D. M. Sussman, E. Kaxiras, and A. J. Liu, A structural approach to relaxation in glassy liquids, Nat. Phys. **12**, 469 (2016).

[46] I. Regev, T. Lookman, and C. Reichhardt, Onset of irreversibility and chaos in amorphous solids under periodic shear, Phys. Rev. E **88**, 062401 (2013).

[47] I. Regev, J. Weber, C. Reichhardt, K. A. Dahmen, and T. Lookman, Reversibility and criticality in amorphous solids, Nat. Commun. **6**, 8805 (2015).

[48] D. Fiocco, G. Foffi, and S. Sastry, Encoding of Memory in Sheared Amorphous Solids, Phys. Rev. Lett. **112**, 025702 (2014).